FULL PAPER

Hierarchical Design for Fabricating Cost-Effective High Performance Supercapacitors

*Nam Dong Kim, D. Bruce Buchholz, Gilberto Casillas, Miguel José-Yacaman, and Robert P. H. Chang**

The salient feature of a supercapacitor is its ability to deliver much higher power density than a battery. A hierarchical design and a cost-effective approach to fabricate high performance supercapacitors using functional carbon nano-particles is reported. A special arc synthesis method is used to produce amorphous/crystalline composite with nitrogen and boron co-doped high charge density carbon nanoparticles. Upon etch removal of the amorphous phase in the composite nanoparticle, a crystalline carbon framework emerges, consisting of a mixture of nano-graphitic sheets mostly in the middle and single nanohorns distributed around the surface of the nanoparticle. These nanoparticles have large internal/external surfaces with subnano channels and sharp nano-tips for high speed charge transport and local charge accumulation. To deliver high power density, the internal resistance of the device is reduced by assembling the nanoparticles via electro-spraying and compacting them into dense films (without any binder) under 700 MPa of pressure before supercapacitor assembly. Taken together, the hierarchical processed supercapacitor has a very high (compared to literature values) power density of nearly 4.5 kW cm^{-3} and a respectable energy density of 2.45 mWh cm^{-3}. Combining these carbon nanoparticles with large area spraying coating, it can lead to a cost-effective production of high performance supercapacitors.

1. Introduction

Advances in the development of renewable energy sources and energy storage systems have propelled the need to design and fabricate ever higher charge-density nanoparticles (HCDN). To this end it is desirable to design a nanostructure with a large surface area for a given total volume or mass. Equally important is the consideration of surface reactivity and the availability of nanoscale channels for atomic/charged species to access internal/external surface sites of the nanostructure. Thus, the big challenge is in the nanostructure architecture where all of these parameters need to be optimized simultaneously. For the case of a supercapacitor, the nanostructure material is used as the framework to store and transport charges between two parallel electrodes. A conventional supercapacitor usually consists of two electrodes (e.g., made of nano-porous carbon materials) with an electrolyte sandwiched between them. In such a configuration an electric double-layer is formed at the interface between the electrolyte and the nanostructure materials of the electrodes. In addition, electrochemical storage can take place at the interfaces, due to the redox reactions which contribute to the pseudo-capacitance of the device.[1]

Over the years, there have been many reports on the use of carbon nanostructure materials for supercapacitor fabrication. They include activated carbon,[2] carbon nanotubes,[3] graphene sheets,[4–6] onion-shaped carbon nano-particles,[7] carbide derived carbon,[8] and templated carbon.[9] In contrast to these studies, our effort is focused on the design and synthesis of functional carbon nanostructures, and the use of a simple process that is scalable for the fabrication of high performance, low cost supercapacitors.

Our hierarchical design and assembly of the HCDN is based on vertically integrating optimal materials-performance at each length scale, ranging from the atomic to micrometers in length. At the atomic level, an abundance of active sites for chemical activity and charge accumulation are needed. At this level, doping the carbon with nitrogen and boron will alter its electronic properties as well as seeding the structural change for the growth of the HCDN during synthesis. At the sub-nano level, abundant channels for efficient mass/charge transport of electrolyte species are needed within the nano-structure. At the nano-structure level, it is necessary to assure that the HCDN has a shape for optimum packing of charges and good electrical contact among the HCDN particles for rapid charge transport. Finally, at the micron level, the HCDN must be assembled and mechanically compacted between the two electrodes to deliver the maximum power density. Thus the elastic properties of the

N. D. Kim, D. B. Buchholz, Prof. R. P. H. Chang
Materials Research Institute & Department of Materials Science and Engineering
Northwestern University
Evanston, IL 60208, USA
E-mail: r-chang@northwestern.edu
G. Casillas, M. José-Yacaman
Department of Physics and Astronomy
University of Texas at San Antonio
one UTSA Circle
San Antonio, TX 78249, USA

DOI: 10.1002/adfm.201304130

© 2014 WILEY-VCH Verlag GmbH & Co. KGaA, Weinheim

HCDN were part of our design consideration. Below we start with the study of HCDN synthesis and characterization at each length scale, and then followed by a discussion on supercapacitor fabrication and its performance.

2. Results and Discussion

2.1. HCDN Fabrication and Structural Analysis

The first goal is to synthesize a HCDN with near spherical shape consisting of doped crystalline frame-work having numerous internal nano-channels and sharp tips for the transport and accumulation of charges. To achieve such an architecture the following two-step processing sequence was taken to synthesize the unique HCDN: First, a composite nanoparticle was synthesized consisting of fine lamella layers of crystalline carbon sandwiched between amorphous layers of nitride and/or carbide materials. Second, the amorphous layers of the composite nanoparticle were selectively etched away by heating the sample in air at 450°C to produce the desired structure.

DC arcs have been extensively used in nano carbon studies.[10–14] To perform the first step, we used a DC arc that was configured as a high temperature furnace where a hole in the cathode serves as a crucible which can be filled with materials to be incorporated into the products.[15] An optimal mixture of 90% graphite powder and 10% B_4C powder was used to synthesize our HCDN particles. B_4C was used primarily as a source for boron doping; nitrogen gas was used as the nitrogen source for co-doping. Our arc was operated with high purity nitrogen at 300 Torr and a temperature around 3000 °C. Under these conditions we obtained a composite HCDN as proposed in step one described above. Nitrides and carbides in our HCDN remain amorphous while carbon achieved its crystalline form. (Note: We have also synthesized HCDN with pure hydrogen and nitrogen gas only. However, the electrical-chemical properties of these samples were inferior, most likely due to their structural properties, thus for this study we only focused on the B-N co-doped samples.

The morphology of the as synthesized B-N co-doped HCDN (BN) collected from the chamber wall is shown in the SEM image, **Figure 1**a. The spherical particles are quite uniform in size, and they range between 40–60 nm. A transmission electron microscopy (TEM) image, Figure 1b, provides a closer view of a cluster of these particles on a holey carbon grid. Figure 1c is a higher magnification of a composite particle showing the crystalline carbon as the matrix embedded with amorphous materials. To study the composition of the as synthesized HCDN, electron energy loss spectroscopy (EELS) was used to map the locations of B, N, and C in the individual particles, and X-ray photoelectron spectroscopy (XPS) was used to study the average amount of each element and their local bonding environment over an assembly of nanoparticles. **Figure 2**a shows a scanning transmission electron microscopy (STEM) image of a selected nano-particle mapped by EELS. STEM images and EELS were acquired in a probe-corrected JEOL ARM200F equipped with a GIF Tridiem operated at 80 kV. The electron energy loss spectrum of the whole nanoparticle clearly shows the B, C, and N edges (Figure 2b). From this mapping (Figure 2c–e) it is clear that both B and N are uniformly present across the nanoparticle indicating that the crystalline and amorphous phases of the composite HCDN are homogeneously distributed within the particle.

In the second step of the synthesis we selectively etch-remove the amorphous materials in the composite HCDN by heating the sample at 450 °C in air. **Figure 3**a is an annular dark field image of a typical nano-particle (BN-1H) after 1 hour of treatment to remove the amorphous material from the nanoparticles. It shows how the dense nano-composite particle has transformed into a nano-porous particle. By further focusing on a single nano-particle (Figure 3b), it is quite revealing to see the transformation of a compact composite nano-particle into a crystalline carbon "skeleton" framework, which consists of densely populated inter-nested carbon nano-horns[16] and twisted nano graphite sheets. The inset to Figure 3b shows the fine structure of a typical nano-horn. An electron diffraction pattern (Figure 3c) was obtained from as deposited BN HCDN (left half circle) and after 1 hour heat treatment, BN-1H (right half circle). The existence of diffraction spots in the rings indicates the presence of randomly oriented carbon crystallites in the BN-1H sample. From the TEM images, it is clear that nano channels have been created within the particle which will improve charge transport. Second, the presence of horn-shaped nano structures will help to induce charging effects around their tips and promote local chemical activities. Thirdly, the inter-connection among the annealed HCDN particles will

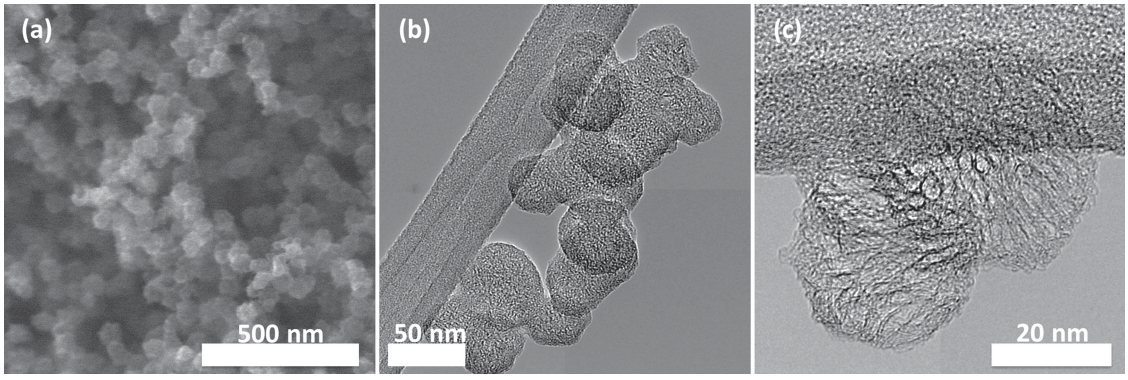

Figure 1. Morphological characterization of as-synthesized BN HCDN. a) High-resolution SEM image of nanoparticles collected from the chamber wall. b) TEM image of a cluster of these nanoparticles on a holey carbon grid. c) High resolution TEM images of as-synthesized BN HCDN.

© 2014 WILEY-VCH Verlag GmbH & Co. KGaA, Weinheim

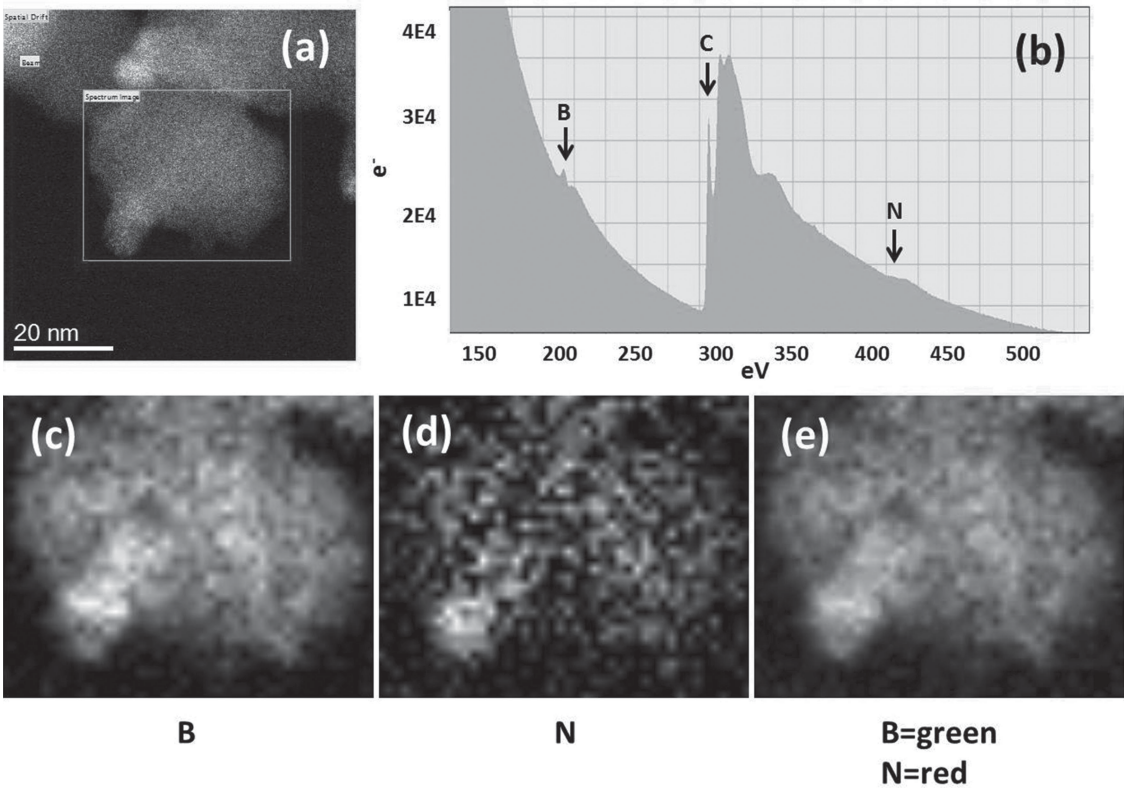

Figure 2. EELS analysis results for the as-synthesized BN HCDN. a) STEM image of a selected BN-HCDN to be mapped by EELS; b) EELS spectrum of particle from (a) showing the B,C, and N edges of EELS; Elemental mapping images of c) B (188–208 eV), d) N (401–421 eV), and e) over lay image.

further enhance the charge flow among the assemblies of these nano-particles.

2.2. Nanoparticle Porosity

While it is clear from the micrographs that selective etching can transform a dense composite HCDN particle into a highly nano-porous crystalline carbon nanoparticle, it is also desirable to quantify the change in porosity that takes place. To this end a Brunauer-Emmett-Teller (BET) pore structure analysis has been carried out. The isotherms are Type II IUPAC classification without adsorption hysteresis (**Figure 4**a). The observed adsorption isotherm appears to be representative of an adsorption isotherm on a flat surface. The etching process results in a remarkably enhanced N_2 adsorption uptake at low relative pressure (P/P_0), which is indicative of a huge increase in nanoporosity. Moreover, continuous N_2 uptake can be observed in the relative pressure range of 0.3–0.6, which also implies the presence of large increase in porosity. The pore size distribution

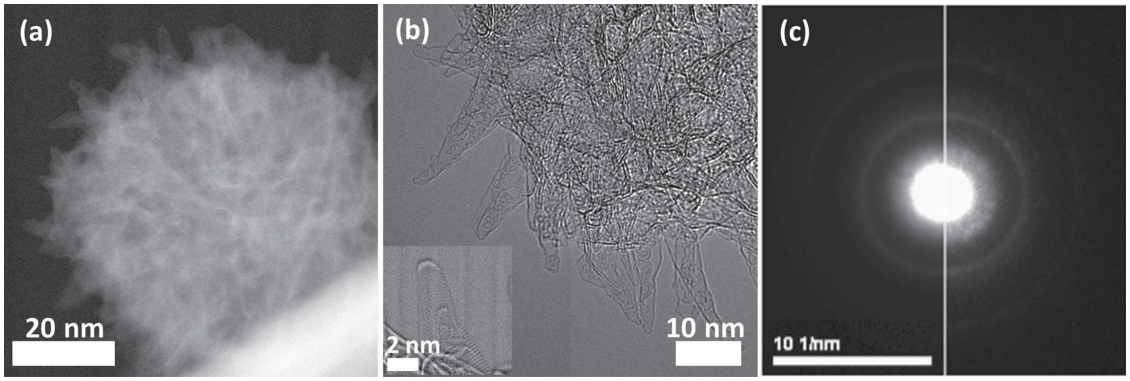

Figure 3. Morphological characterization of annealed BN-HCDN (BN-1H). a) High resolution annular dark field-STEM images, and b) bright field high resolution STEM images of single BN-1H particle. c) Comparison of electron diffraction patterns between as-synthesized BN HCDN (left) and BN-1H (right). Bright spots in the right half indicate graphitic (crystalline) characteristics of BN-1H, compared with the hazy pattern of as-synthesized BN HCDN in the left half.

© 2014 WILEY-VCH Verlag GmbH & Co. KGaA, Weinheim

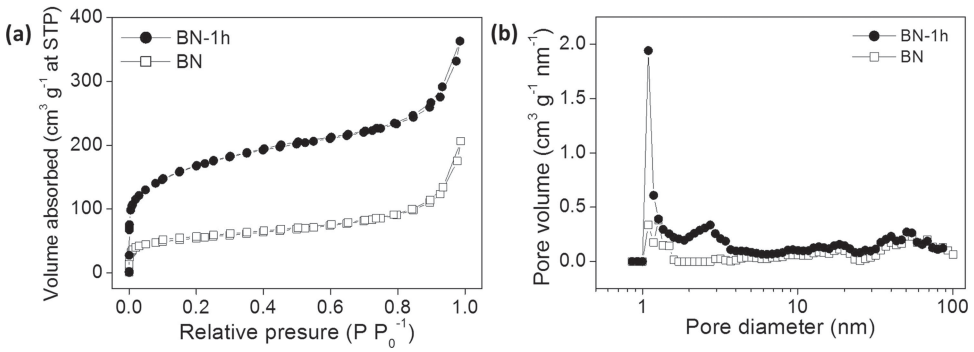

Figure 4. Porosity analysis from the BET measurement. Gas adsorption/desorption analysis using N2 (77.4 K) of the BN HCDN before and after the annealing process. a) High-resolution N2 isotherms, and b) pore-size distribution (calculated by using a slit NLDFT model).

was calculated using the quenched solid density functional theory (QSDFT) method that was part of the Quarda Win software package (Quanta chrome Instruments, USA), assuming a slit pore geometry. From this analysis there is only a minor amount of pores with characteristics in the micropore range for the as synthesized BN sample. On the other hand, there are two obvious peaks in the micropore range for the etched sample: one very sharp peak just above 1 nm and another broad peak (with one tenth the height) between 2–3 nm (Figure 4b). This dramatic increase in pore volume around 1 nm can be attributed to the presence of numerous nano and/or sub-nano channels formed by the intertwined nano-carbon layers and nano-horns left behind in the etched nano-particle discussed above[17,18]. As a result, the surface area and pore volume of the etched sample increase over the unetched sample from 193.3 $m^2 g^{-1}$ to 554.3 $m^2 g^{-1}$, and from 0.27 $cm^3 g^{-1}$ to 0.51 $cm^3 g^{-1}$, respectively. It should be pointed out here that these values remain nearly the same after our HCDN film is compacted with a pressure of 700 MPa.

2.3. XPS Analysis

Extensive XPS studies were performed on our BN and BN-1H particles. From the survey spectrum of the N and BN samples (**Figure 5**a) indicates the incorporation of N and B into these materials. The nitrogen and boron concentrations in the as grown co-doped sample, BN, are about 4 at% and 3 at% respectively (**Table 1**). The predominate asymmetric C 1s peak, shown in Figure 5b, indicates the existence of C–N, C–B, and/or C–O bonds in addition to C–C bonds. The C 1s spectrum could be deconvoluted into four peaks at 283.5, 284.7, 286.3,

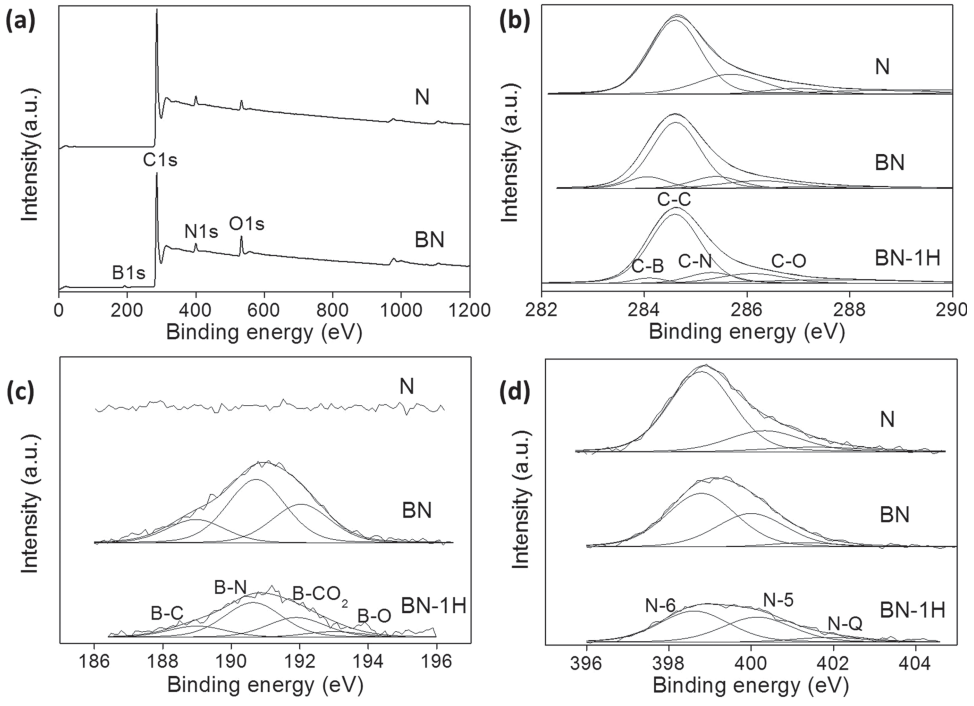

Figure 5. XPS spectrum analysis for the N, BN, and BN-1H samples. a) survey spectrum and high resolution spectrum of b) C 1s, c) B 1s, and d) N 1s.

© 2014 WILEY-VCH Verlag GmbH & Co. KGaA, Weinheim

Table 1. Summarize XPS peak analysis for N, BN, and BN-1H samples.

sample	C[a]				B[b]					N[c]			
	C–B	C–C	C–N	C–O	Content	B–C	B–N	$B–CO_2$	B–O	content	N-6	N-5	N-Q
N	-	60.9%	21.1%	18.0%	-	-	-			4.0 at%	71.7%	21.8%	6.5%
BN	6.7%	69.7%	13.2%	10.4%	3.0 at%	18.7%	50.5%	30.8%	-	4.1 at%	58.8%	36.6%	4.6%
BN-1h	3.6%	72.3%	10.5%	13.5%	0.8 at%	15.7%	48.7%	27.7%	7.9%	2.2 at%	41.1%	51.1%	7.8%

[a]C–B (283.4 eV), C–C (284.6 eV), C–N (286.2 eV), and C–O (288.3 eV); [b]B–C (189.5 eV), B–N (190.6eV), $B–CO_2$ (192 eV), and B–O (193 eV); [c]N-6 (Pyridinic-398.5 eV), N-5 (Pyrrolic-400.5 eV), and N-Q (Quaternary-401.2 eV).

and 288.4 eV; these were assigned to C–B, sp^2 C=C, C–N, and/or C–O bonds, and π–π sp^2 satellite transitions respectively.[19–25] The B1s core level can be divided into maximum 4 peaks of B–O (193 eV), BCO_2 (192 eV), B–N (190.6 eV), and B–C (189.5 eV) (Figure 5c).[20,26,27] The relatively large amount of B-N bonding indicates that N from the reaction gas reacts preferentially with B over C when B is present. The high resolution N 1s peak can be deconvoluted into 3 components (Figure 5d); N-6 (398.6 eV), N-5 (400.6e V), and N-Q (401.6 eV).[20,24] N-6 corresponds to pyridinic substitution in the carbon lattice, N-5 to pyrrolic substitution in the carbon lattice and/or B–N bonding, and N-Q to graphitic substitution in the carbon lattice. Considering large amount of B–N bonding indicated from the B 1s spectra, it can be assumed that there are also large amount of N–B bonding, along with the pyrrolic N substitution, in peak N-6 in the B doped samples. As depicted above, due to the nature of ternary mixture in BN sample, there are large amount of different bonding at lower binding energy comparing with N sample (including N-6 and N-5). Although the amount of B and N were somewhat decreased by the 1h annealing, sufficient quantities of B (0.8 at%) and N (2.2 at%) remain to change the surface chemistry of the BN-1h sample thereby increasing its electrochemical activities. Moreover, it should be noted that most of the nitrogen species present are aspyridinic (N-6) and pyrrolic (N-5) substitution. This is because nitrogen can act as an edge termination agent during the graphene growth in a role similar to hydrogen in a hydrogen arc growth.[24] These N-6 and N-5 species are favorable for accumulating charges during supercapacitor operation due to their appropriate electron configuration and binding energy.[28] Nitrogen bonding around the nano-graphitic edges favors pyridinic substitution[24]; density function theory (DFT) calculation indicates this should produce a p-type material.[29] XPS also indicates pyrrolic N-substitution where the Fermi level is in the middle of the gap. After annealing in air, the amount of oxygen species (such as hydroxyl, ester, ketone, and carboxylic groups) on the surface of the HCDN were slightly increased from ≈7 at% to 10 at%. Addition of these groups further enhances the redox reaction for more charge accumulation, and also increases the hydrophilic surface property for better wettability of the materials, which eventually increase the overall electrochemical performance of BN-1H HCDN [30] (see Supporting Information SI-1). We also show the difference in surface wettability of these samples with contact angle measurements (see Supporting information SI-4). Indeed, the BN-1H sample has the best wettability.

2.4. HCDN Sample Densification

The HCDN nano-particles were compacted or densified into a film under uniaxial pressure for the fabrication of supercapacitors. The densification of the HCDN film is needed to optimize the device performance to obtain both the highest energy density and power density. This requires the optimization of at least two important parameters: charge density (amount of charge per volume) stored in the capacitor, and the supercapacitor charging and discharging rate (which requires the minimization of internal resistance of the device). In addition, the device needs to possess long term stability through cycling. Densification is thus a key step to achieving these properties. To assure that we do not over-compress the nano-particle film (beyond its elastic limit), we performed in-situ nano-indentation measurements on single selected BN-1H HCDN particles in a HR-TEM (see SI-2, Supporting Information). An AFM-TEM in situ holder from Nanofactory AB was used to perform the compression experiments.[31,32] Briefly, the nanoparticles are drop-casted onto an Au wire, which is mounted in to the AFM-TEM holder and once inside the TEM, they are compressed by a Si tip (Supporting Information Figure SI-2.1). The deflection of the cantilever is used to compute the load applied on the particles and the area of contact is estimated from the TEM images. Our results showed that a single nanoparticle was able to withstand ≈1000 MPa of stress at the contact point without any deformation (except for the sharp tips, Figure SI-2.2, Supporting Information). Beyond this stress the nanoparticle started to compress plastically. According to these results, we used an uniaxial pressure of 700 MPa to ensure that the nanoparticles were not damaged in the film formation process discussed below (see Supporting Information Figure SI-2.3, BET isotherm result for compressed BN-1H sample).

2.5. Electrical Measurement

We performed Hall measurements on normally ≈300 μm thick BN-1H co-doped HCDN films. The films were formed by compacting the HCDN particles under a uniaxial pressure of 700 MPa. The Hall mobility was determined to be ≈2 $cm^2\ V^{-1}\ s^{-1}$ with a p-type carrier density of $5 \times 10^{19}\ cm^{-3}$ to yield a conductivity of ≈15 $S\ cm^{-1}$. This carrier density is about one order of magnitude higher than an N-doped sample grown in the nitrogen arc without boron doping, while the p-type mobility is the same. Thus, the BN co-doped sample is more conductive by roughly a factor of 10 (see more detail in SI-3, Supporting Informa-

© 2014 WILEY-VCH Verlag GmbH & Co. KGaA, Weinheim

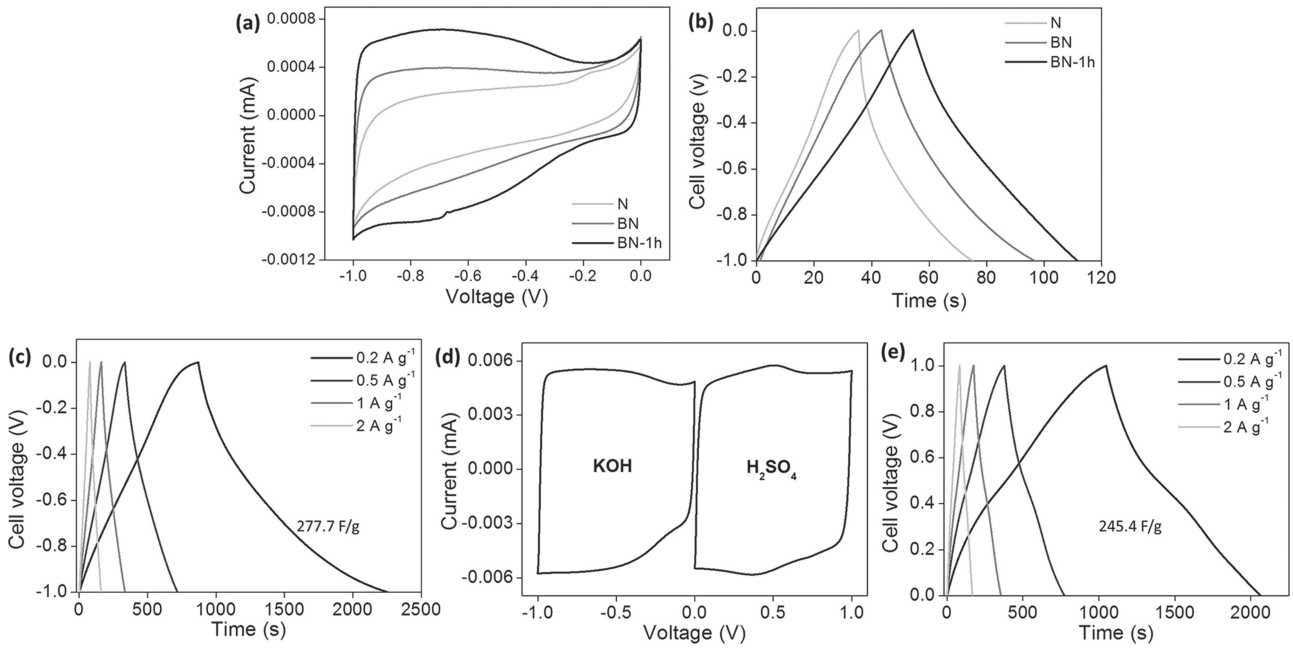

Figure 6. Electrochemical characterization in three electrode configuration. a,b) Comparison study among the samples of N, as-synthesized BN, and BN-1H; a) CV curves measured in 6 M KOH electrolyte from –1.0 to 0 V at 100 mV s^{-1} and b) Galvanostatic charge/discharge profiles at the current density of 3 A g^{-1}. c–e) In depth study of BN-1H. d) CV curves obtained in different electrolyte systems of 6 M KOH and 1 M of H_2SO_4 at scan rate of 1 V s^{-1}. Galvanostatic charge/discharge profiles at different current densities obtained in c) 6 M of KOH, and e) 1 M of H_2SO_4.

tion). This information is very important to the design of our supercapacitor. To achieve high rates of charging and discharging, the internal resistance of the device needs to be very low.

2.6. Electrochemical Analysis

As a demonstration of the advantage of its unique structure, the electrochemical activity of B-N co-doped HCDN material was compared with N-doped HCDN samples using a three-electrode cell. **Figure 6**a shows typical cyclic voltammograms (CV) for a three-electrode cell in 6 M KOH at a scan rate of 100 mV s^{-1}. The as-deposited BN HCDN exhibits a much larger CV curve than the N sample corresponding to superior electrochemical activities for storing charges. Considering the similar values for surface area (193.3 m^2 g^{-1} for the BN sample and 215 m^2 g^{-1} for the N sample), the increase in electrochemical activity is attributed to the synergetic effect of B–N co-doping in the carbon structure as discussed earlier. Sharp response at the voltage changing point represents the fast charge/discharge characteristics owing to the favorable surface chemical properties of B–N co-doping effects. Heteroatom doping in the carbon framework changes the electronic properties of the material with the heteroatoms being more favorable for the attraction of ions in the electrolyte compared to that of the carbon atoms, thus inducing pseudocapacitance.[28] Additionally, the presence of heteroatoms in the carbon matrix can enhance the wettability (hydrophilicity) between electrolyte and electrode materials (See SI-4 for contact angle experiment).[33] Therefore, the heteroatom doping could not only introduce extra pseudocapacitance but also enhance the electric double-layer capacitance. The B–N co-doped synergetic effect becomes more significant after 1 h annealing process. Due to the highly increased conductivity of the BN-1H sample relative to the BN sample, faster response can be obtained resulting in a nearly rectangular shaped CV curve. Moreover, characteristics of the redox reaction became more obvious showing the appearance of "humps" in the CV curves (Figure 6a). Capacitive behaviors can also be observed, exhibiting linear behavior during the galvanostatic charge/discharge experiments performed at 3 A g^{-1} (Figure 6b). The specific capacitance of BN-1H sample was calculated from the discharging curves with values of as high as 277 F g^{-1} at a current density of 0.2 A g^{-1}.

For the further validation of the advantages of B-N co-doping, an electrochemical activity test was also performed in acidic media (1 M of H_2SO_4). Figure 6c shows charging/discharging scans as a function of current for 6 M KOH solution, while Figure 6e shows that for 1 M H_2SO_4 solution. Figure 6d compares the differences in the electrolyte solutions in *C*–*V* plots. The specific capacitance of the BN-1H was calculated from galvanostatic charge/discharge curves according to the relation $C_{spec} = Itm^{-1}V^{-1}$, where *I* is the charge/discharge current, t is the discharge time, *m* is the mass of electrode material, and *V* is the voltage difference. The highest capacitance values, calculated from the discharge curves, were 277 F g^{-1}, and 245 F g^{-1} in 6 M KOH and 1 M H_2SO_4, respectively (see Supporting Information SI-4 for detail discussion about the different electrochemical behavior in KOH and H_2SO_4 electrolyte). Considering the surface area (554.3 m^2 g^{-1}), this value can be converted to a considerably high value of 49.9 μF cm^{-2} which is much higher value than 10–30 μF cm^{-2} which are typically showed in carbon materials.[34,35] This means the BN-1H has highly electrochemical-active surface characteristics.

© 2014 WILEY-VCH Verlag GmbH & Co. KGaA, Weinheim

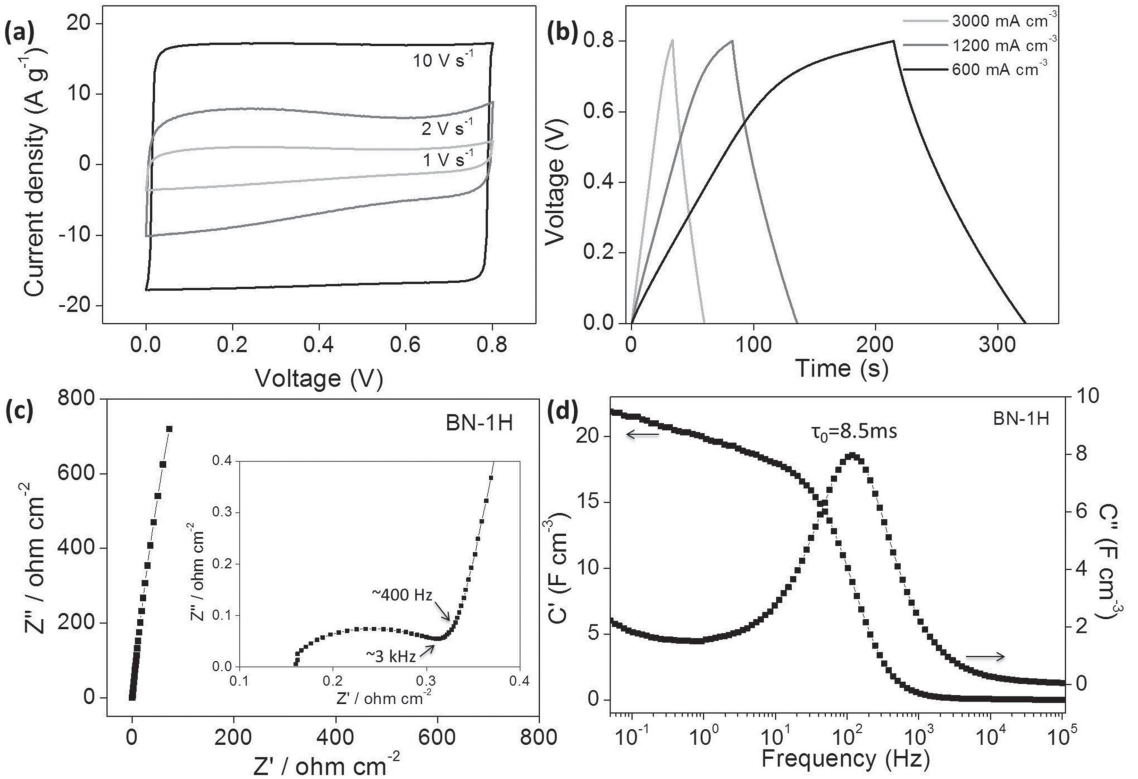

Figure 7. Electrochemical characterization of thin film supercapacitor. a) CVs profiles of a thin film supercapacitor of BN-1H in a 6 M KOH, at different scan rates, from low to high. b) Galvanostatic charge/discharge curves at different current densities. c) Complex plane plot of the impedance analysis, with a magnification for the high-frequency region in the inset. d) The real and imaginary part of the capacitance (*C′* and *C″*) as a function of frequency. Very low relaxation time constant τ_0 (8.5 ms) is confirmed.

2.7. Fabrication and Properties of Two-Electrode Supercapacitor

Based on the above results it is clear that BN-1H particles have superior electro-chemical properties and thus should be used for the fabrication of the two-electrode supercapacitors. The steps taken to prepare the devices are as follows (see Supporting Information SI-5): BN-1H carbon nanoparticles processed from the arc furnace as describe above are electro-sprayed onto two identical stainless steel substrates to form thin films of BN-1H. In order to retain high efficiency (low internal resistance), no organic binding material has been used in assembly the BN-1H nanoparticles. The thin films are further compacted under a pressure of 700 MPa to a thickness of ≈1 µm. The two densified electrodes are sandwiched together mechanically with a polypropylene separator layer between them. This assembly is then soaked in the 6 M of KOH electrolyte. **Figure 7** shows the characteristics of a typical supercapacitor. Cyclicvoltammograms (CVs) were recorded at scan rates from 1000 mV s^{-1} to 10 000 mV s^{-1} to test the power capability of the thin film supercapacitor (Figure 7a). Almost perfect rectangular shaped CV curves, up to the very high scan rate, indicate low resistance, as well as its high power characteristics for the device. The galvanostatic charge/discharge curves at three current densities are shown in Figure 7b. The specific capacitance was calculated from the discharge curves with values of 28.3, 28.1, and 28.1 F cm^{-3} obtained at current densities of 600, 1200, and 3000 mA cm^{-3}, respectively (Figure 7b).

Electrochemical impedance spectroscopy (EIS) further confirms the superior power performance of the compacted BN-1H thin film supercapacitor. The vertical feature in the Nyquist plot of BN-1H shows the nearly ideal capacitive behavior of the cell. The equivalent series resistance obtained from the intercept of the plot on the real axis is only 0.34 Ω cm^{-2} (compared with few hundreds of ohms of un-compacted film, Supporting Information, Figure SI-6.1). From the expanded high-frequency range data (Figure 7c, inset), a transition between the RC semicircle and the migration of electrolyte was observed at a frequency ≈3000 Hz. The diffusion of electrolyte ions stopped ca. 400 Hz, and thereafter the full capacitance was reached. The thin film supercapacitor of BN-1H shows superior frequency response with a very small relaxation time constant τ_0 of 8.5 ms (τ_0 being the minimum time needed to discharge all the energy from the device with an efficiency of greater than 50%; [36] Figure 7d). This small time constant for BN-1H is very promising compared with previously reported values for planar micro-supercapacitors: activated carbon (700 ms),[7] onion-like carbon (26 ms) [7] and direct laser writing graphene device (19 ms).[5] The measured electrical properties of the BN-1H two electrode supercapacitor gives a high power density (4.58 kW cm^{-3}) and energy density (2.45 mWh cm^{-3}). Furthermore, the thin film BN-1H supercapacitors show excellent cycling stability, retaining ≈90% of the initial performance after 10 000 charge/discharge cycles (Supporting Information-Figure SI-7.1).

© 2014 WILEY-VCH Verlag GmbH & Co. KGaA, Weinheim

3. Conclusion

In summary, we have reported a cost-effective approach to fabricate high performance supercapacitors using specially designed and processed nitrogen and boron co-doped carbon HDCN. This requires the assembly of closely interconnected nanoparticles with large internal/external surfaces and plenty of subnano channels for high speed charge transport. To improve the power density, we reduced the internal resistance of the device by forming the supercapacitor under 700 MPa of uniaxial pressure. Taken together our integrated approach provided us with a power density of nearly 4.58 kW cm^{-3}, highest reported to date in the literature to our knowledge. In addition, a respectable energy density of 2.45 mWh cm^{-3} was also obtained. The described fabrication process can be easily scalable for manufacturing.

4. Experimental Section

Synthesis of Boron and Nitrogen Doped Arc Carbon Materials: The arc system used in this study is described in detail elsewhere.[37] Briefly, the arc consists of two electrodes. The cathode is a solid 3/8 inch diameter randomly oriented graphite (ROG) rod. The anode is a cup-like structure fabricated from a 3/8 inch diameter ROG rod with a 3/16 inch diameter hole, 4 inch deep, in the center of the end facing the cathode. The hole, or cup, in the anode cup is filled with tightly compacted graphite powder; as a boron (B) source 10 wt% B_4C was mixed with graphite powder.

After the chamber was evacuated, 300 Torr of Nitrogen (N) gas was introduced. Nitrogen was used as nitrogen source. A 100 Amp DC arc was applied to heat the graphite powder inside the hole. A potential of 27–28 V was maintained between the electrodes by adjusting the spacing between them, typically 0.5 to 0.7 inch. A typical synthesis experiment lasts ≈7 min. The arc soot deposited on the surface of chamber was collected.

There are some graphite impurities in the as-collected soot, so a purification process was performed to remove un-desired carbon species. First, the as-collected sample was dispersed in a solution of water and ethanol (9:1) and then sonicated to make a highly dispersed suspension. The suspension was centrifuged to remove heavy graphitic balls from the arc soot. After the centrifugation, the supernatant was freeze-dried overnight to yield the purified arc soot. This sample is designated as the as-synthesized BN HCDN in this paper (Supporting Information, Figure SI-8.1). For the control experiment, pure graphite powder without B_4C addition, was introduced into the arc discharge process to produce soot doped with only nitrogen, which is designated as the N sample.

For the synthesis of the BN-1H sample, as-synthesized carbon soot underwent aheat treatment in air at 450 °C to etch-remove of the amorphous portion of the material.

Characterization of Synthesized Materials: Scanning electron microscopic (SEM) images were obtained using a Hitachi SU8030 field emission SEM (FESEM). Transmission electron microscopy (TEM), selected area electron diffraction (SAED) studies were performed using a JEOL 2100F FAST TEM working at 200 kV. Structural characterization of the arc carbon was done by X-ray diffraction (XRD, D/MAX-A, Rigaku) featuring Jade Analysis software. The surface area and pore size distribution of the synthesized HCDN were measured by nitrogen adsorption/desorption isotherms, using a Micromeritics ASAP 2020 system. The sample was degassed at 398 K under vacuum overnight before analysis, to remove any adsorbed impurities. The surface area was measured using the Brunauer–Emmett–Teller (BET) model for relative pressures and the distribution of pore dimensions was calculated using the Barrett–Joyner–Halenda (BJH) model. XPS spectra were recorded on a Thermo Scientific ESCALAB 250Xi. All binding energies (BEs) are referred to the graphitic C 1s line at 284.7 eV.

Compressing Test for the BN-1H Sample: The in situ TEM experiments were performed in a JEOL JEM-2010F. Images were recorded with an AMT CCD camera. The sample was diluted in ethanol, ultrasonicated and drop-casted on to a 0.25-mm Au wire that was mounted on an N force probing holder (AFM-TEM holder) from Nanofactory Instruments AB. The sample is mounted on a piezotube which enables three-dimensional movement with sub-nanometer precision. For load measurements, this holder relies on the deflection of a silicon cantilever with a sharp tip. Supporting Information Figure SI-2.1 shows a picture of the actual holder used. These experiments were carried out with a cantilever of a spring constant of 2.3 nN m^{-1}. Finally, the stress can be estimated by assuming a circular area of contact and measuring the diameter from the TEM images.

Three-Electrode Test: Electrochemical measurements were performed using an AUTOLAB PGASTAT 302N potentiostat with a standard three-electrode setup in both 6 M of KOH and 1 M H_2SO_4. Working electrodes were prepared by drop-casting the samples on a glassy carbon electrode: A Pt plate and an Ag/AgCl electrode saturated with KCl were used as a counter electrode and reference electrode, respectively. Cyclic voltammograms were recorded within the range from 0 to –1 V in KOH and from 0 to 1 V in H_2SO_4 at various scan rates. Galvanostatic charge/discharge was carried out within the same voltage range of CV measurement at various current densities. Electrochemical impedance spectroscopy (EIS) measurement was carried out by applying voltage amplitude of 10 mV at OCV (open circuit voltage) in the frequency range from 100 kHz to 50 mHz.

Calculations: The capacitance of each device was calculated from the galvanostatic charge/discharge curves using the formula:

$$\text{For a three electrode configuration: } C_{\text{electrode}} = \frac{i \times \Delta t}{\Delta V}$$

Where i (A) is the discharge current, Δt (s) is the discharge time, ΔV (V) is the voltage change (excluding the iR drop) within the discharge time. Gravimetric specific capacitance was calculated by dividing capacitance by the mass of electrode material.

$$\text{For a two electrode thin film configuration: } C_{\text{device}} = \frac{i \times \Delta t}{\Delta V} \times 4$$

Where i (A) is the discharge current, Δt (s) is the discharge time, ΔV (V) is the voltage change (excluding the iR drop) within the discharge time, the multiplier of 4 adjusts the capacitance of the cell and the combined mass of two electrodes to the capacitance and mass of a single electrode. Specific capacitance was calculated based on the volume of the device according to the following formula:

$$\text{Volumetric capacitance } (C_v) = C_{\text{device}} / V$$

where V refers to the volume (cm^3) of the device.

The energy density (Wh cm^{-3}) and power density (W cm^{-3}) derived from the charge/discharge curves are calculated by the following equations;

$$E = C_v \times \Delta V^2 / (2 \times 3600)$$

$$P = \Delta V^2 / 4 R_{ESR} V$$

For the calculation of maximum power density, R_{ESR}(equivalent series resistance) of the device was obtained from the EIS (Electrochemical impedance spectroscopy) measurements.

Acknowledgements

The authors would like to thank Shiqiang Li, Dr. Aiming Yan, and Prof. V. Dravid for diffraction measurements, Dr. Jaemyung Kim and Prof. Jiaxing Huang for help with measuring the electrochemical

© 2014 WILEY-VCH Verlag GmbH & Co. KGaA, Weinheim

performance, Dr. Jinkuen Park and Prof. Joseph T. Hupp for the porosity measurements, and Dr. Hyo Seon Suh and Prof. Paul Nealey for the contact angle measurements. The authors would like to acknowledge funding from NSF-IMI program DMR-0843962, Northwestern University ISEN program GL008, and the NSF-PREM Grant # DMR 0934218: "Oxide and Metal Nanoparticles – The Interface between Life Sciences and Physical Sciences"

Received: December 10, 2013
Revised: February 4, 2014
Published online: April 2, 2014

[1] G. Z. Chen, *Prog. Nat. Sci. Mater.* **2013**, *23*, 245.
[2] J. A. Fernandez, T. Morishita, M. Toyoda, M. Inagaki, F. Stoeckli, T. A. Centeno, *J. Power Sources* **2008**, *175*, 675.
[3] L. Ci, S. M. Manikoth, X. Li, R. Vajtai, P. M. Ajayan, *Adv. Mater.* **2007**, *19*, 3300.
[4] Y. Zhu, S. Murani, M. D. Stoller, K. J. Ganesh, W. Cai, P. J. Ferreira, A. Pirkle, R. M. Wallace, K. A. Cychosz, M. Thommes, D. Su, E. A. Stach, R. S. Ruoff, *Science* **2011**, *332*, 1537.
[5] M. F. El-Kady, R. B. Kaner, *Nat. Commun.* **2013**, *4*, 1475.
[6] Z. S. Wu, K. Parvez1, X. Feng, K. Müllen, *Nat. Commun.* **2013**, *4*, 2487.
[7] D. Pech, M. Brunet, H. Durou, P. Huang, V. Mochalin, Y. Gogotsi, P-L. Taberna, P. Simon, *Nat. Nanotechnol.* **2010**, *5*, 651.
[8] J. Chmiola, C. Largeot, P-L. Taberna, P. Simon, Y. Gogotsi, *Science* **2010**, *328*, 480.
[9] W. Kim, J. B. Joo, N. D. Kim, S. Oh, P. Kim, J. Yi, *Carbon* **2009**, *47*, 1407.
[10] V. P. Dravid, X. Lin, Y. Wang, X. K. Wang, A. Yee, J. B. Keterson, R. P. H. Chang, *Science* **1993**, *259*, 1601.
[11] X. K. Wang, X. W. Lin, V. P. Dravid, J. B. Ketterson, R. P. H. Chang, *Appl. Phys.Lett.* **1995**, *66*, 2430.
[12] N. Li, Z. Wang, K. Zhao, Z. Shi, Z. Gu, S. Xu, *Carbon* **2010**, *48*, 255.
[13] B. Lee, D. B. Buchholz, R. P. H. Chang, *Energy Environ. Sci.* **2012**, *5*, 6941.
[14] X. Lin, X. K. Wang, V. P. Dravid, R. P. H. Chang, J. B. Ketterson, *Appl. Phys. Lett.* **1994**, *64*, 181.
[15] S. P. Doherty, D. B. Buchholz, R. P. H. Chang, *Carbon* **2006**, *44*, 1511.
[16] M. Yudasaka, S. Iijima, V. H. Crespi, *Carbon nanotub.* **2008**, *111*, 605.
[17] S. Bandow, F. Kokai, K Takahashi, M. Yudasaka, L. C. Qin, S. Iijima, *Chem. Phys. Lett.* **2000**, *321*, 514.
[18] S. Utsumi, J. Miyawaki, H. Tanaka, Y. Hattori, T. Itoi, N. Ichikuni, H. Kanoh, M. Yudasaka, S. Iijima, K. Kaneko, *J. Phys. Chem. B* **2005**, *109*, 14319.
[19] S. Maldonado, S. Morin, K. J. Stevenson, *Carbon* **2006**, *44*, 1429.
[20] W. J. Hsieh, S. H. Lai, L. H. Chan, K. L. Chang, H. C. Shih, *Carbon* **2005**, *43*, 820.
[21] P. Hammer, N. M. Victoria, F. Alvarez, *J. Vac. Sci. Technol. A* **2000**, *18*, 2277.
[22] H. Valdés, M. Sánchez-Polo, J. Rivera-Utrilla, C. A. Zaror, *Langmuir* **2002**, *18*, 2111.
[23] K. László, E. Tombácz, K. Josepovits, *Carbon* **2001**, *39*, 1217.
[24] Y. C. Lin, C. Y. Lin, P. W. Chiu, *Appl. Phys. Lett.* **2010**, *96*, 133110.
[25] S. T. Jackson, R. G. Nuzzo, *Appl. Surf. Sci.* **1995**, *90*, 195.
[26] Y. Kang, Z. Chu, D. Zhang, G. Li, Z. Jiang, H. Cheng, X. Li, *Carbon* **2013**, *61*, 200.
[27] S. H. Sheng, H. L. Gao, W. J. Bao, F. B. Wang, X. H. Xia, *J. Mater. Chem.* **2012**, *22*, 390.
[28] F. M. Hassan, V. Chabot, J. Li, B. K. Kim, L. Ricardez-Sandoval, A. Yu, *J. Mater. Chem.A* **2013**, *1*, 2904.
[29] D. Usachov, O. Vilkov, A. Grüneis, D. Haberer, A. Fedorov, V. K. Adamchuk, A. B. Preobrajenski, P. Dudin, A. Barinov, M. Oehzelt, C. Laubschat, D. V. Vyalikh, *Nano Lett.* **2011**, *11*, 5401.
[30] M. Inagakia, H. Konnoa, O. Tanaike, *J. Power Sources* **2010**, *195*, 7880.
[31] G. Casillas, J. P. Palomares-Báez, J. L. Rodríguez-López, J. Luo, A. Ponce, R. Esparza, J. J. Velázquez-Salazar, A. Hurtado-Macias, J. González-Hernández, M. José-Yacaman, *Philos. Mag.* **2012**, *92*, 4437.
[32] G. Casillas, A. Ponce, J. J. Velazquez-Salazar, M. Jose-Yacaman, *Nanoscale.* **2013**, *5*, 6333.
[33] E. Iyyamperumal, S. Wang, L. Dai, *ACS Nano* **2012**, *6*, 5259.
[34] L. L. Zhang, X. S. Zhao, *Chem. Soc. Rev.* **2009**, *38*, 2520.
[35] J. Han, L. L. Zhang, S. Lee, J. Oh, K-S. Lee, F. R. Potts, J. Ji, X. Zhao, R. S. Ruoff, S. Park, *ACS Nano* **2013**, *7*, 19.
[36] P. Banerjee, I. Perez, L. Henn-Lecordier, S. B. Lee, G. W. Rubloff, *Nat. Nanotechnol.* **2009**, *4*, 292.
[37] L. S. Wang, D. B. Buchholz, Y. Li, J. Li, C. Y. Lee, H. T. Chiu, R. P. H. Chang, *Appl. Phys. A* **2007**, *87*, 1.

© 2014 WILEY-VCH Verlag GmbH & Co. KGaA, Weinheim